Progress In Electromagnetics Research B, Vol. 81, 101–122, 2018

FMCW Radar System for Transponder Identification

Nizar Bouhlel[1], Stéphane Méric[1, *], Claude Moullec[2], and Christian Brousseau[3]

Abstract—In this paper, we deal with a frequency modulated continuous wave (FMCW) radar used for localizing and tracking targets by frequency evaluation of the received radar beat signal. The radar system achieved with a primary radar (reader) and a secondary radar (transponder) is addressed as super high frequency (SHF) radio frequency identification (RFID). Consequently, considering the transponder as an active target, we achieve an identification application thanks to the shift frequency induced by the transponder. Moreover, the impact of the non-linearity behavior of this transponder on the localization performance is investigated, and a solution is proposed for cancelling non-linear effects.

1. INTRODUCTION

The frequency-modulated continuous wave (FMCW) radars are systems transmitting a continuous and frequency modulated waveform [1]. These radars transmit and receive simultaneously and without interruption unlike modulated pulsed radars. The FMCW radars are widely used for industrial and academic with many useful applications [2]. The advantages of the FMCW radars are multiples: excellent performance for near-distance applications, excellent range resolution, no blind distance [1, 3], easy implementation, low power consumption, miniaturized system design, simplicity and low cost. Particularly, for near-target detection, the FMCW radar is an alternative to the impulse radar [4] as there no limitation for transmitting pulsewidth and for switching time between transmission an reception. An FMCW radar is used to locate targets [2, 8, 9] since it can detect the ranges and velocities of objects. The FMCW radars are also used in other applications such as snow thickness measurement [5], imaging application -SAR imagery [2]-, terrain displacement monitoring [6], as well as automotive applications in collision avoidance [7].

Another way to remotely detect objects is the use of the radio frequency identification (RFID) systems. The RFID allows identification and tracking of persons or objects. Over the last decade, RFID systems have received a great attention due to their simple architecture, smaller dimensions, low-cost, low-power and ease of deployment. The RFID systems operating at HF range are used in several applications such as access control, livestock tracking, etc. With the technological advances of RFID (efficient broadband wireless electronics, integration techniques) it is possible to operate with UHF and SHF range allowing a larger operating distance [10, 11]. It is this progress that new application areas open such as tracking of persons or objects, bio-signal recording [12], logistics monitoring [13] and environmental sensing [14]. Two types of RFID systems are still used nowadays: passive and active. On the one hand, passive UHF transponders can operate up to a distance of 10 meters. On the other hand, active transponders with their own battery allow higher distances for detection and characterization applications. Therefore, besides the standard data transfer function between reader and transponder, distance information could also be evaluated [15]. In the case of active configuration, the connected object is considered as a cooperative target. Also, identification and localization of this

---

Received 20 March 2018, Accepted 28 May 2018, Scheduled 7 July 2018

* Corresponding author: Stéphane Méric (stephane.meric@insa-rennes.fr).

[1] Univ. Rennes, INSA Rennes, CNRS, IETR, UMR 6164, Rennes F-35000, France. [2] ADVANTEN, 30 route de Fougères, Cesson-Sévigné, France. [3] Univ. Rennes, CNRS, IETR, UMR 6164, Rennes F-35000, France.

kind of cooperative target such as RFID backscatter transponder, is well-known for a long time. Thus, we can combine the RFID concept that considers the target as an active device to radar systems which can evaluate the received radar beat signal for localizing and tracking targets.

In this paper, we deal with the system GESTAR (GEnerator System for TArget Radar identification). This system is a radar system for detecting and localizing cooperative targets in complex environments (urban areas, buildings, forests, snow). The system is composed of a small reader (the primary radar) and a shift frequency identification transponder (the secondary radar) responding to the primary radar only when this latter produces an interrogation signal. Indeed, the primary radar transmits an FMCW that is received by the transponder. The FMCW signal is characterized by a RF carrier frequency, a transmitted power and a frequency sweep. The transponder re-transmits this signal by introducing its own shift frequency. The power transmitted by the transponder is captured by the primary radar, signal processed, and the target (transponder) is then precisely located by using a constant false alarm rate (CFAR) detection. Finally, the reader displays on a small screen the position (radial distance), the angular position and the shift frequency of the targets. The particularity and innovation of GESTAR is the absence of blind distance as well as the great autonomy of the transponder. The performances of this system are characterized by several parameters namely: the range resolution, the shift frequency resolution, the angle estimation accuracy and the maximum range detection capacity.

Two kinds of transponders are manufactured and used for this study. The first kind of transponder linearly modulates the re-transmitted signal to the primary radar by adding a shift frequency. The other one operates a nonlinear modulation. The primary radar is tested either with a linear, or with a nonlinear transponders. Good results are obtained for the linear transponder in the sense that we correctly detect targets. Nevertheless, the beat signal is modified when the nonlinear transponder is used and thus the range-shift frequency cartography is altered as well. This alteration is caused by the presence of several harmonics that are added to the spectrum and caused by the aliasing. Therefore, the identification of the target becomes difficult. We propose in this paper to study the effect of non-linearity behavior of the transponder in the detection and localization. Moreover, we present a method to remove the undesirable harmonics validated by simulations and measurements.

The paper is organized as follows. Section 2 introduces the principles of RFID localization based on FMCW signal. The FMCW radar performances are presented in Section 3. Next, the FMCW radar implementation is presented in Section 4. The content of Section 5 is related to the non-linearity behaviors of the transponder and the consequences on the detection and localization. Finally, Section 6 concludes this paper.

2. RFID LOCALIZATION BASED ON FMCW SIGNAL

2.1. Principle of Modulated Backscattering

Figure 1 shows the principle of the RFID localization system using an FMCW radar system. The primary radar system transmits a signal $s_e(t)$ assumed to be a linear frequency modulated signal in

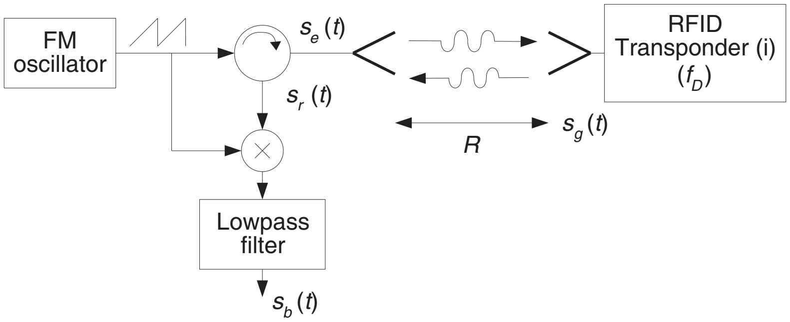

Figure 1. Setup of FMCW radar based RFID localization system.

time interval $[0, T]$. The analytic expression of $s_e(t)$ is given as follows

$$s_e(t) = A_e \exp \jmath 2\pi \left(f_0 t + \frac{B}{2T} t^2 \right) \tag{1}$$

where A_e, f_0, B, and T denote respectively the amplitude, the RF carrier frequency, the sweep bandwidth, and the sweep duration which can also be considered as the modulation duration. In the case of the RFID transponder located at a distance R from the radar that modulates the carrier frequency through a shift frequency f_D, the RFID is considered as a secondary radar. This secondary radar transmits the signal $s_g(t)$ given as follows

$$s_g(t) = K A_e \exp \jmath 2\pi \left(f_0 \left(t - \frac{R}{c} \right) - f_D t + \frac{B}{2T} \left(t - \frac{R}{c} \right)^2 \right) \tag{2}$$

where the parameter K represents the attenuation coefficient with respect to the radar equation (propagation effect, antenna gains and so on), and c is the velocity of the wave. In the same way, the received signal by the radar $s_r(t)$ is an attenuated (K' parameter) and delayed version of the transmitted signal with a delay of $\tau = 2R/c$. Therefore, the received signal is given as follows

$$s_r(t) = K' A_e \exp \jmath 2\pi \left(f_0 (t - \tau) - f_D \left(t - \frac{\tau}{2} \right) + \frac{B}{2T} (t - \tau)^2 \right) \tag{3}$$

The principle of a homodyne demodulation of the received signal consists in mixing the signal $s_e(t)$ with the received signal $s_r(t)$. The expression of the beat signal at the mixer output is $s_b(t) = s_e(t) s_r^*(t)$ where (*) denotes the conjugate operator. The delay between the transmitted signal and the received signal results in a constant beat frequency called f_b which makes possible to measure the distance between the target (transponder) and the radar (reader). The beat signal is given as follows

$$s_b(t) = K' A_e \exp \jmath 2\pi \left(\left(\frac{B\tau}{T} - f_D \right) t + \phi_0 \right) \tag{4}$$

where $\phi_0 = f_0 \tau - B\tau^2/(2T) - f_D R/c$ is a constant phase. A more detailed calculation for $s_b(t)$ is provided with Appendix A. As shown in Fig. 2(a), we define t_c as the time description over the sweep duration T. The time axis t_l is defined as a time data set that collects one sample for each T duration: $t_l = mT$ with $m = 0, 1, \ldots, M-1$ where M is the total number of modulation duration (see Fig. 2(b)). On the one hand ($f_D = 0$), we define the beat frequency f_b by

$$f_b = \frac{B}{T} \tau = \frac{2BR}{cT} \tag{5}$$

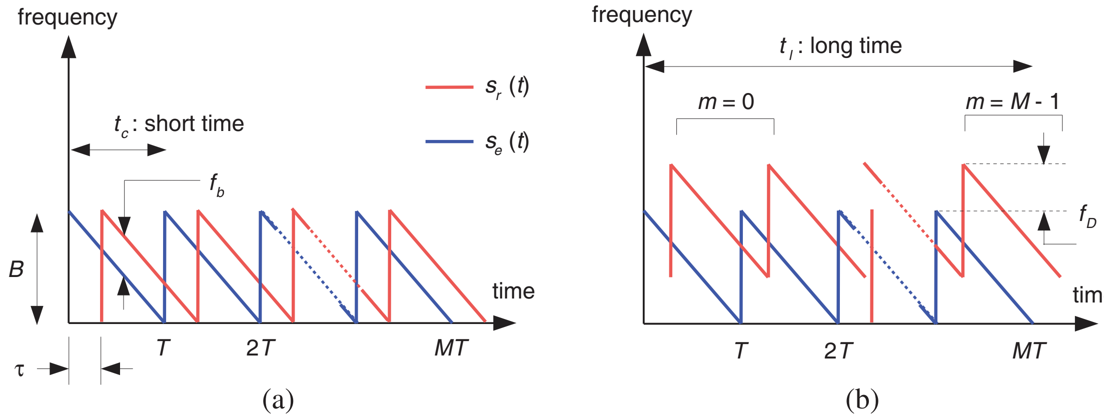

Figure 2. Beat signal over several modulation duration T with respect to shift frequency f_D. (a) Case of $f_D = 0$. (b) Case of $f_D \neq 0$.

and the f_b value extracted during each modulation duration T allows the determination of R. On the other hand, in the case of a frequency shift f_D modulation ($f_D \neq 0$), an FMCW radar can also be measured f_D by integrating data from several cycles of wave replication over the long time axis (Fig. 2(b)). Consequently, the beat signal $s_b(t)$ could be described with respect to both the time axes t_c and t_l [10].

$$s_b(t_c, t_l) = K'' A_e e^{\jmath 2\pi\phi'_0} e^{\jmath 2\pi f_b t_c} e^{\jmath 2\pi f_D mT} \tag{6}$$

where $\phi'_0 = \phi_0 + B\tau m$. To establish the range-shift frequency cartography, the beat signal analysis is carried out in the Fourier domain and also two Fourier transforms need to be applied. A more detailed description of specific Fourier transform is addressed hereafter in Section 4.1. Moreover, we apply a specific signal processing to separate the range information (extracted from f_b) from the shift frequency identification (extracted from f_D) as we explain in Section 3.4.

In the case of continuous time Fourier analysis over the t_c axis, the first Fourier transform denoted $S_b^c(f, t_l) = TF[s_b^c(t_c, t_l)](f)$ is calculated for $\tau_{\max} < t_c < T$ where the c exposant means the continuous case, and $\tau_{\max}$ corresponds to the delay for a maximum distance. The expression of $S_b^c(f, t_l)$ is given as follows

$$S_b^c(f, t_l) = K'' A_e\, e^{\jmath 2\pi\phi'_0} \times (T - \tau_{\max}) e^{\jmath 2\pi f_D t_l} \times e^{-\jmath\pi(f-f_b)(T+\tau_{\max})} \mathrm{sinc}\left(\pi(f - f_b)(T - \tau_{\max})\right). \tag{7}$$

It is clear that the maximum of $S_b^c(f, t_l)$ is reached when $f = f_b$. The application of the second Fourier transform over the t_l axis for shift frequency processing where $0 < t_l < (M-1)T$ is given as follows

$$\begin{aligned} S_b^c(f, f') \;=\; & K'' A_e\, e^{\jmath 2\pi\phi'_0} \times (T - \tau_{\max}) e^{-\jmath\pi(f-f_b)(T+\tau_{\max})} \mathrm{sinc}\left(\pi(f - f_b)(T - \tau_{\max})\right) \\ & \times (M-1) T e^{-\jmath\pi(f'-f_D)(M-1)T} \mathrm{sinc}\big(\pi(f' - f_D)(M-1)T\big) \end{aligned} \tag{8}$$

The expression given by Equation (8) which is the two-dimensional Fourier transform of the beat signal makes possible to draw up a range-shift frequency cartography where we can identify targets by their distances and their shift frequency.

In the case of discrete-time signal description, the beat signal is now sampled. The short time t_c is described according to the sampling frequency F_e and the long time t_l according to the period repetition frequency $F_s = 1/T$. The discrete-time Fourier transform, which is connected to the Fourier transform in the continuous case by the Poisson formula, is given as follows

$$\begin{aligned} S_b(f, f') \;=\; & F_e F_s \sum_{n=-\infty}^{\infty} \sum_{k=-\infty}^{\infty} S_b^c(f - nF_e, f' - kF_s) = F_e F_s (T - \tau_{\max})(M-1) T e^{\jmath 2\pi\phi'_0} \\ & \times \sum_{n=-\infty}^{\infty} e^{-\jmath\pi(f-nF_e-f_b)(T+\tau_{\max})} \mathrm{sinc}[\pi(f - nF_e - f_b)(T - \tau_{\max})] \\ & \times \sum_{k=-\infty}^{\infty} e^{-\jmath\pi(f'-kF_s-f_D)(M-1)T} \mathrm{sinc}[\pi(f' - kF_s - f_D)(M-1)T]. \end{aligned} \tag{9}$$

The details of calculation are given in Appendix B.

2.2. Angular Analysis

In the case of GESTAR system, the primary radar has 2 receive antennas. Thus, it is possible to measure the angular position of targets. A phase comparison monopulse method [16] is used to estimate the angular position of the targets in the horizontal plane. This method consists in measuring the phase difference ϕ observed between the two receiving channels:

$$\frac{\Delta}{\Sigma} = -\jmath \tan\left(\frac{\phi}{2}\right) \tag{10}$$

where Δ and Σ are the difference and sum, respectively, of the responses of the target on the two receiving antennas. The measured phase ϕ is related to the horizontal separation d of the two antennas and the position θ of the target as shown in Fig. 3.

$$\phi = 2\pi \frac{d}{\lambda} \sin(\theta). \tag{11}$$

Determining ϕ allows us the estimation of the angular position θ of the target.

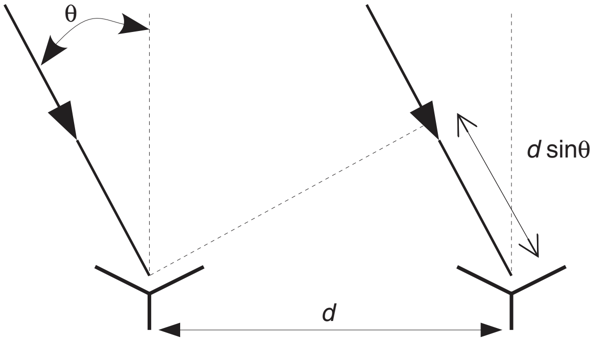

Figure 3. Angular position estimation.

3. FMCW RADAR PERFORMANCES

In our case, the radar performances are set up through range resolution and frequency resolution. These resolutions depend upon sweep duration, sweep bandwidth, and pre-processing of the data. In the following subsections, we define the range and shift frequency resolutions. We also achieve some simulations corresponding to the range-shift frequency cartography and angular position cartography.

3.1. Range Resolution

The range resolution is defined as the smallest distance between two targets of the same power that can be separated by the processing [18]. For a homodyne FMCW radar, the range resolution can be represented by [19]

$$\Delta R = \frac{cT}{2B}\Delta f_b \tag{12}$$

where Δf_b is the beat frequency resolution which is proportional to the observation time of the signal processed, i.e., for the beat signal:

$$\Delta f_b = \frac{1}{T - \tau_{\max}}. \tag{13}$$

Then, the resolution can be written $\Delta R = c/(2B)$. It is clear that the time modulation T does not affect the range resolution as long as it remains much greater than $\tau_{\max}$.

3.2. Shift Frequency Resolution

The shift frequency f_D induced by the RFID transponder is measured by taking into account the beat signal over M sweep durations [1]. Assuming the displacement of the RFID transponder less than the range resolution, a discrete Fourier transform (DFT) procedure is carried out on axis time t_l to estimate the shift frequency f_D. Thus, the shift frequency resolution Δf_D is inversely proportional to the processed signal observation time and

$$\Delta f_D = \frac{1}{MT}. \tag{14}$$

By increasing the time modulation T the shift frequency resolution decreases meaning that this resolution is improved.

3.3. System Parameters

The specific parameters that characterize our radar system are provided in Table 1. These are the main parameters of radio transmission, modulation, signal processing, transponder and CFAR detection. To investigate the radar performance and argue the requested maximum visible range (285 m), a power balance study is required. For this, we need the theoretical received power allowing reliable detection

Table 1. Simulation setup parameters.

Radio	Carrier frequency f_c	5.8 GHz
	Transmitter power P_e	25 mW PIRE
	Antenna gains G_e, G_r	12 dBi
	Receiver noise factor F	5 dB
Antenna	Type	3D antenna
	Distance between antenna (d)	0.8λ
Modulation	Type	Sawtooth
	Frequency Sweep B	60 MHz
	Ramp duration T	80 µs
	Total number M	1600
Signal Processing	Sampling Frequency F_e	20 MHz
	Nb. points (range)	1530 points
	Nb. points (shift frequency)	1600 points
	Total time MT	128 ms
Transponder	Radar cross-section σ	$-10\,\mathrm{dBm}^2$
	Shift frequency f_D	[19 kHz–21 kHz]
CFAR	Noise type	Gaussian
	SNR detection	13 dB
	probability of false alarm P_{fa}	10^{-3}
	probability of the detection P_d	0.9

of targets in a Gaussian noise. Indeed, the reflected power of the RFID transponder, denoted P_r at the location R of the primary radar antenna, is related to the transmitted power P_e and is given by the following radar equation [16]:

$$P_r = P_e \frac{G_e G_r \lambda^2 \sigma}{(4\pi^3)\, R^4 L} \tag{15}$$

where G_e and G_r stand for the gain of the transmitting and receiving antennas of the FMCW primary radar, $\lambda = c/f_0$ the system wave length in free space, R the distance between the reader (primary radar) and the transponder (secondary radar), σ the radar cross section of the transponder considered as a target, and L the loss factor. As the acquired signal can be extremely low, reception amplification stages are needed to operate the data received by the primary radar. The amplification chain introduces noise that is added to the received signal. The average power of the thermal noise in reception is defined by:

$$P_n = K_b T_0 B_n F \tag{16}$$

where K_b is the Boltzman's constant, T_0 the temperature of the receiving chain, F the noise factor, and B_n the received bandwidth of the radar. In our case, the average noise power P_n is given for $B_n = 20\,\mathrm{MHz}$, $T_0 = 290\,\mathrm{K}$ and $F = 5\,\mathrm{dB}$, and is equal to -96 dBm. In the presence of Gaussian noise, a signal-to-noise ratio (SNR) of 13 dB is required to obtain a probability of detection, denoted P_d of 0.9 with false alarm probability $P_{fa} = 10^{-3}$. The SNR = 13 dB is the value used to estimate the radar detection capability [17]. This value allows to determine the detection capability of the radar under very favorable conditions (free space).

The processing gain of GESTAR system is a function of the number of analysed points N. Moreover, we apply a Nuttall window as a weighing function on the beat signal defined by (6). The processing gain is weighted by the normalized equivalent noise bandwidth (NENBW) [20] which is equal to 1.9761 for the Nuttall window. Then, the processing gain is $P_{GR} = 10\log_{10}(1530/\mathrm{NENBW}) = 28.89\,\mathrm{dB}$ for a range analysis and is $P_{GD} = 10\log_{10}(1600/\mathrm{NENBW}) = 29.08\,\mathrm{dB}$ for the shift frequency analysis.

Moreover, the global processing P_G is given by

$$P_G = P_{GR} + P_{GD} \tag{17}$$

The received power P_r from the RFID transponder below which the detection probability value is too low, is obtained by

$$P_r = 13 - P_G + P_n = -140.8\,\text{dBm} \tag{18}$$

From (15) we can also deduce the corresponding maximum visible range R_{mvr}. Fig. 4 shows the power balance for maximum visible range. Based on (14) the shift frequency resolution is equal to $\Delta f_D = 7.8\,\text{Hz}$ with 1600 points spread over the interval [0, 12.5 kHz] or [12.5 kHz, 25 kHz]. The resolution of the shift frequency analysis is degraded by the Nutall window used in this study. Then, the resolution at $-6\,\text{dB}$ is given by $2.627/MT = 20.52\,\text{Hz}$ where 2.627 corresponds to the normalized width of the main lobe of the Nutall window. For the range resolution, it is given by $\Delta R = c/2\,B = 2.5\,\text{m}$. As mentioned before, this resolution is degraded by the use of Nutall windows, and then the resolution at $-6\,\text{dB}$ is given by $2.627 \times \Delta R = 6.567\,\text{m}$. Table 2 shows the performance provided by the radar as function of the parameters of Table 1.

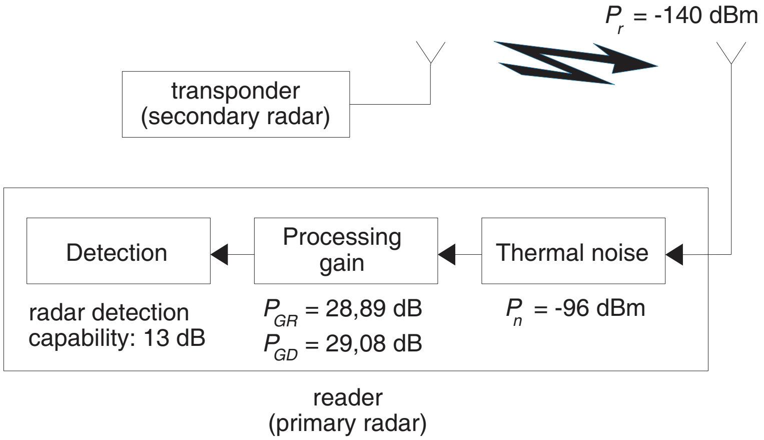

Figure 4. Power balance for maximum visible range $R_{mvr} = 285\,\text{m}$.

Table 2. Radar performances achieved.

Detection ability	
SNR	$\geq 13\,\text{dB}$
Maximum visible range	285 m
Time detection	400 ms
Range estimation	
Measuring range	[0–500 m]
Resolution	2.5 m
Resolution at $-6\,\text{dB}$	6.87 m
Shift frequency estimation	
Resolution	7.8 Hz
Resolution at $-6\,\text{dB}$	20.52 Hz
Angular estimation	
Measuring range	from -15 deg. to 15 deg.

3.4. Simulations

First of all, as the shift frequency range is given (see Table 1), an average frequency compensation of 20 kHz is performed regardless of the value of the frequency shift introduced by the transponder. A maximum error of ±1 kHz is thus committed that corresponds of a ±0.2 meter error on the range distance of the transponder. This error which is much lower than the range resolution, is considered negligible.

We perform simulations with the parameters given in Table 1. We establish the range-shift frequency cartography and the angular position cartography. Fig. 5(a) shows the detection of 3 targets (T#1, T#2 and T#3) with radial distances [50, 150, 200] m for T#1, T#2 and T#3 respectively.

Moreover, the shift frequency values of [20, 20.2, 20.6] kHz characterize T#1, T#2 and T#3 respectively. The targets are located at angles $\theta = [\pi/30, \pi/20, 0]$ which are measured in the azimuth plane. From Fig. 5, it is clear that the targets are correctly detected and the estimated ranges and shift frequencies correspond to the real ranges and frequencies. The detection level decreases when the target are far from the radar as it is shown with the T#3 target where $R = 200\,\text{m}$. It is also indicated by the power P_r given by (15) which is inversely proportional to the distance R. Fig. 5(b) shows the estimation of the angular position of the targets. The angular position is computed as follows: for each detected target in range-shift frequency cartography, we use Equations (10) and (11) to compute θ. The quality of the estimated angular position depends on the distance between target and radar, and is highly affected by the noise. Target T#1 and T#3, where $R = 50\,\text{m}$ and $R = 200\,\text{m}$, are correctly estimated unlike target T#2 that the angular position is not right.

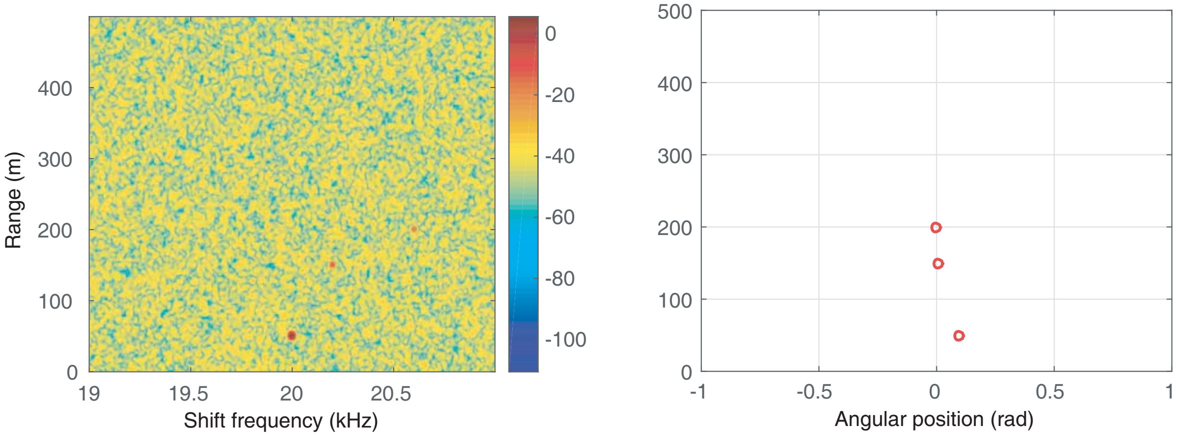

(a) (b)

Figure 5. Example of detection of 3 targets with distances [50, 150, 200] m with respective shift frequencies [20, 20.2, 20.6] kHz. The targets are oriented at angles measured with respect to the vertical $\theta = [\pi/30, \pi/20, 0]$ radian. (a) Range-shift frequency cartography. (b) Range-angular cartography.

4. FMCW RADAR IMPLEMENTATION

The radar uses a transmitting antenna and two receiving antennas to allow estimation of the angular position of the targets. Since the transmission and reception are simultaneous, we have maintained high isolation to reach good detection performance. In this section, we present the radar system design with different components. Fig. 6 shows a block diagram of the various modules that compose the radar system. It mainly consists of a power supply module, a signal processing module, transmission and reception modules, and an antenna system. In the following subsections, we present these modules.

4.1. Signal Processing and Display

The signal processing module is implemented in a field-programmable gate array (FPGA) board which is the core of this module. This board accommodates an ALTERA Cyclone V FPGA, a dual 16-bit digital-to-analog converter, a quad 16-bit analog-to-digital converter, a low power double data rate 2 (LPDDR2) memory, and interface circuits. The FPGA is responsible for generating the radar signal transmitted by the radio module, processing the signal received by the two radio reception chains to detect the presence of the transponders, identifying their shift frequency, locating them by estimating their radial distance and their angular position and display the corresponding information on the organic light-emitting diode (OLED) screen of the radar (Fig. 7). To enable real-time radar analysis, most of the processing

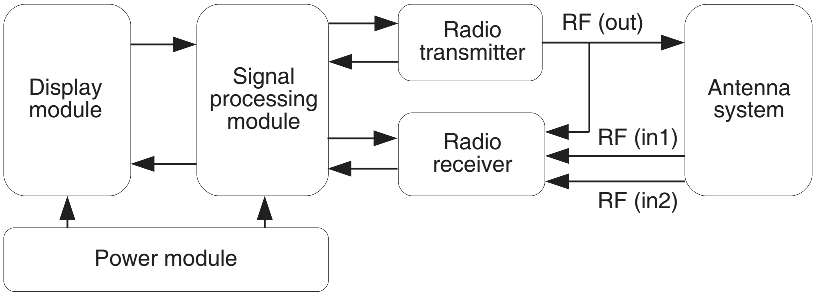

Figure 6. Block diagram of the various modules that composes the radar system.

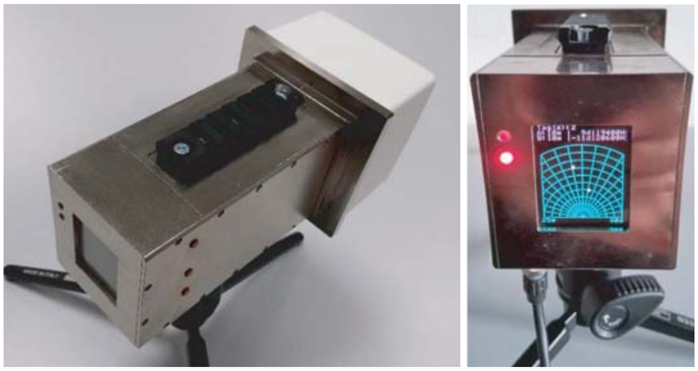

Figure 7. The designed radar equipped with an OLED display.

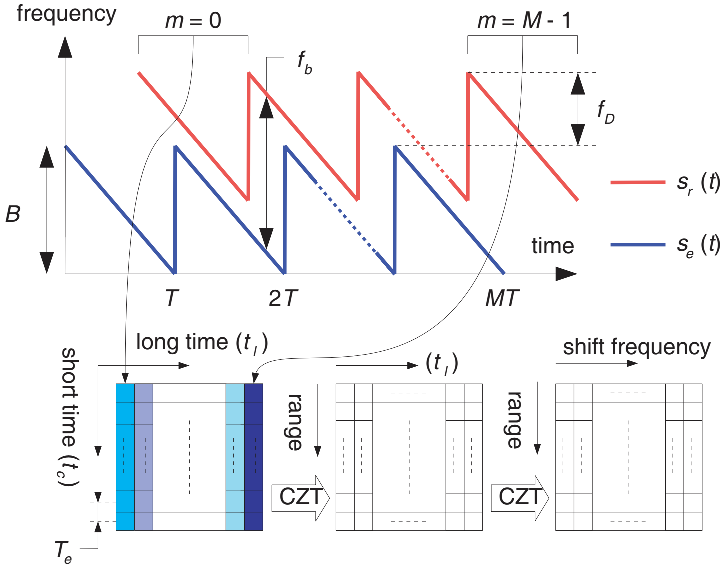

Figure 8. Instantaneous frequency over M transmitted ramps.

procedures required for these operations is carried out by dedicated hardware functions implemented in the FPGA and controlled by a 32-bit microprocessor (Nios II System Controller). The algorithms based on simple or regular control structures are achieved through hardware implementation such as the algorithms of distance frequency analysis and shift frequency analysis as well as the estimation of the noise level for the detection threshold determination. Algorithms with a complex control structure benefit from a software implementation, such as the algorithm for detecting targets, estimating their parameters and managing the radar display. This structure makes it possible to reduce the time required for the detection of the transponders and the estimation of their parameters to a value of less than 200 ms. The implementation of the spectrum analysis of the beat signal is realized via a chirp Z-transform (CZT) which is the Z-transform of a signal along a spiral contour [21, 22]. The advantage of CZT is to evaluate the beat signal frequency only in a zone of interest $[F_{\min}, F_{\max}]$. The user can define the number of analysis point that makes possible to improve the frequency resolution.

We illustrate in Fig. 8 the different steps for achieving a range-shift frequency cartography from the samples of the beat signal given by (6). These samples are collected and positioned into a matrix: each line represents the short time dimension and each column gives the long time dimension. The first CZT distance is applied to each column to form a distance profile matrix. The column number k of this new matrix represents the distance profile of the chirp number k. The second CZT is applied to each line for shift frequency processing. The output of this second CZT provides the radar operator with range-shift frequency cartography from the scene.

4.2. Radio Transmitter and Receiver

This part consists in selecting components allowing to realize the basic functions of the radio chains (amplification, filtering, transposition of frequency, ...). Some basic functions are realized thanks to printed structures optimized in simulation with the Microwave Office simulator. Fig. 9 shows a band pass filter which is optimized by simulation.

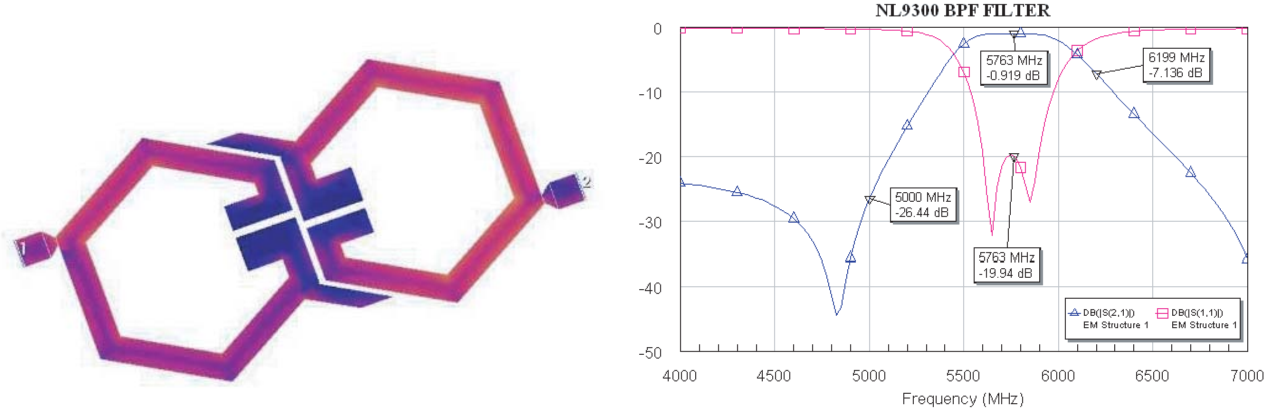

Figure 9. Optimized bandpass filter by simulation.

A radio module consisting of a transmission board and a two-way reception board is made as exhibited in Fig. 10. The two radio boards are assembled in a nickel-plated aluminum shielding mechanism with a lower cover, a separation shield (Fig. 10(b)) and a top cover. The assembled radio module (Fig. 10(d)) is in the form of a parallelepiped with dimensions 90 × 55 × 25.2 mm and weights 122 g. The transmission board (Fig. 10(a)) performs frequency synthesis functions and radio frequency transposition, amplification and filtering of the radar signal provided on two channels in quadrature by the signal processing module. A portion of the transmitted signal is picked up and supplied to the receiving board to perform the homodyne demodulation of the received signal. The reception board (Fig. 10(c)) comprises two identical radio reception chains consisting of the following main functions: filtering, low noise amplification, quadrature demodulation, variable gain amplification.

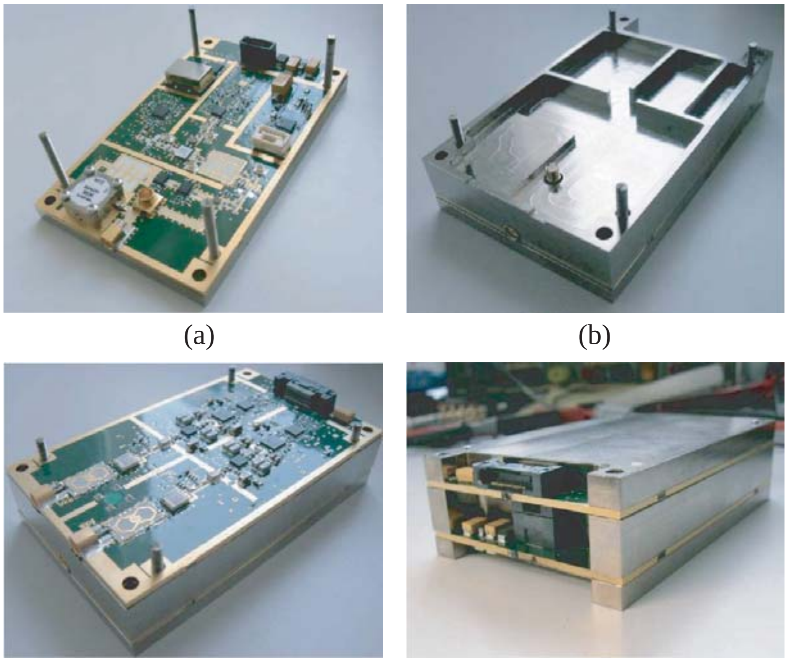

(a) (b)

(c) (d)

Figure 10. Radio module with transmission and receiving boards.

4.3. Antenna

As this paper is not dedicated to the antenna studies, we only slightly describe the antenna performances.

The study of antennas firstly include selecting the type of radiating element to achieve the specifications about the volume available for the antennas on the artwork of the radar. The choice is thus made on axial-mode helical antennas with circular polarization capable of offering a directivity and a quality of polarization compatible with the specifications for three channels in a reduced volume. The selected compact antenna device is studied and optimized in simulation using the CST Microwave Studio software. Fig. 11(a) shows the compact antenna device with three radiating elements. One element is dedicated to the transmission and the other two to the reception. This compact antenna with radome is measured in an anechoic chamber as shown in Fig. 11(b).

As a conclusion for this part, we summarize the antenna performances and characteristics from the measurements, shown in Table 3.

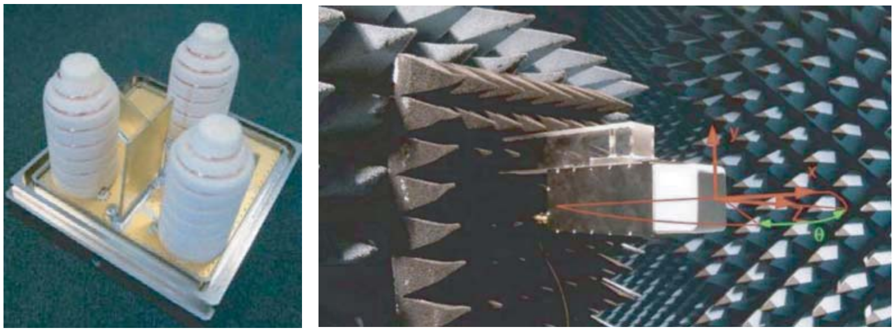

(a) (b)

Figure 11. (a) The realized compact antenna device with three radiating elements and (b) the front radiation patterns measured in an anechoic chamber, as a function of the orientation angle θ.

Table 3. Main characteristics of the antenna.

Distance between antenna	0.672λ
Transmitted antenna	
Transmitter gain	9.4 dBi
Transmitter beamwidth (H plane)	47 deg.
Received antenna	
Receiver gain	9.4 dBi/8.4 dBi
Receiver beamwidth	63 deg./77 deg.
Transmitter and receiver isolation	−43 dB/−40 dB

4.4. Measurement Results

Indoor and outdoor measurements are achieved for free-space propagation with the radar (primary and secondary) system as outlined above. We expose range, shift frequency and orientation angle values and take over 1500 measurements in indoor context. Fig. 12(a) shows the distance and estimated shift frequency. The estimated values of distance and shift frequency which are respectively 15 m and 20.6 kHz match the ground truth. Fig. 12(b) exhibits the measured orientation angle where the ground truth value is 1 degree. It is clear that the variance of this parameter is low and that the average is close to the true value. This fluctuation is justified by the presence of noise that affects the estimation of this parameter. Moreover, the monopulse angle estimation is based on data measures from two antennas and does not take into consideration any prior knowledge about the nature of noise. Finally, the Fig. 12 shows the values of the SNR as a function of the number of measurements. The SNR decrease with respect to the number of measurements is small. Nevertheless, this decrease is explained by the depletion of the transponder batteries.

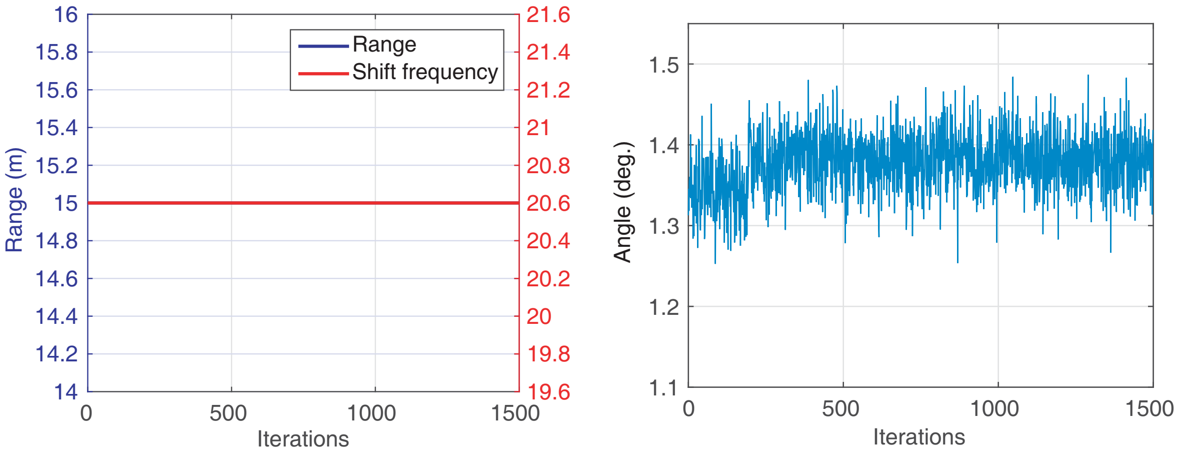

(a) (b)

Figure 12. (a) Range and shift frequency indoor measurements and (b) orientation angle indoor measurement curves.

For outdoor configuration, we achieve measurements with the transponder located at 25 m from the radar and identified by a shift frequency of 20.6 kHz. The Fig. 14 corresponds to the range-shift frequency cartography we obtain thanks to the signal processing described in Section 4.1. As depicted in Fig. 14, the output values of this range-shift frequency cartography give a distance of 25 m for the transponder and a shift frequency of 20.6 kHz.

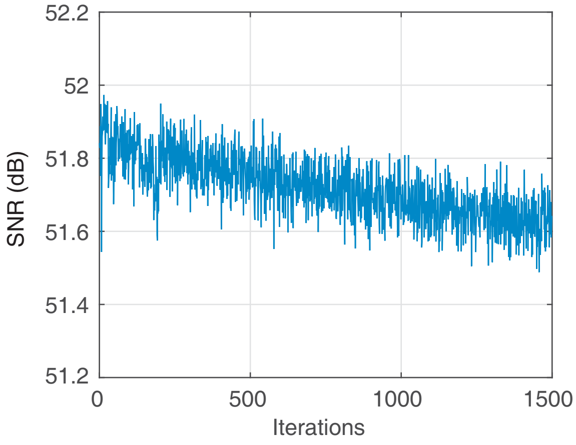

Figure 13. Evolution of the SNR (dB) with respect to the number of measurements.

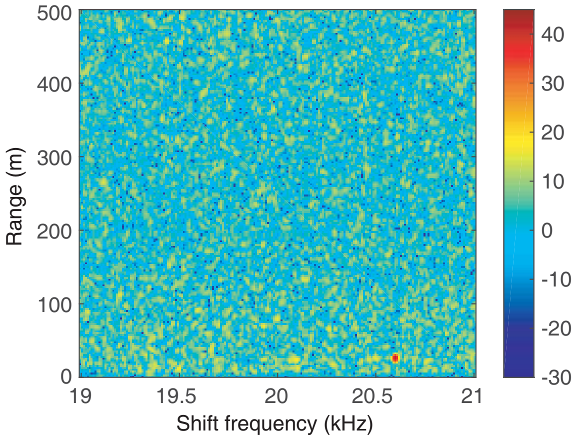

Figure 14. Range-shift frequency cartography established for a single target at distance $R = 25\,\mathrm{m}$ from the radar with a transponder shift frequency $f_D = 20.6\,\mathrm{kHz}$.

5. NONLINEAR EFFECTS

This section describes the non-linearity behavior of the transponder and the consequences on the detection and localization. The range measurement with the nonlinear transponder is presented and a solution is given to eliminate undesirable harmonic effects. These effects could be considered as target and could be seen as false alarm.

5.1. Nonlinear Modulation Effect in Time Domain

In a linear approach, the transponder is characterized by the frequency shift f_D which is added to the transmitted signal from the reader part of the system as described in Section 2.1. The nonlinear modulation that we use in this study is exhibited in Fig. 15. The transponder receives the radar signal $s_e(t-\tau)$ and then modulates this received signal by its proper signal $g(t)$. The waveform $g(t)$ is considered as the transponder characteristic. For our study, we propose to modelize the nonlinear transponder effect with an alternative periodic signal $g(t)$. The period of $g(t)$ is $1/f_D$. Fig. 15(b) shows $g(t)$ as function of time. Since $g(t)$ is periodic, we can derive it into Fourier series

$$g(t) = \sum_{n=-\infty}^{+\infty} C_n \exp(j2\pi n f_D t) \tag{19}$$

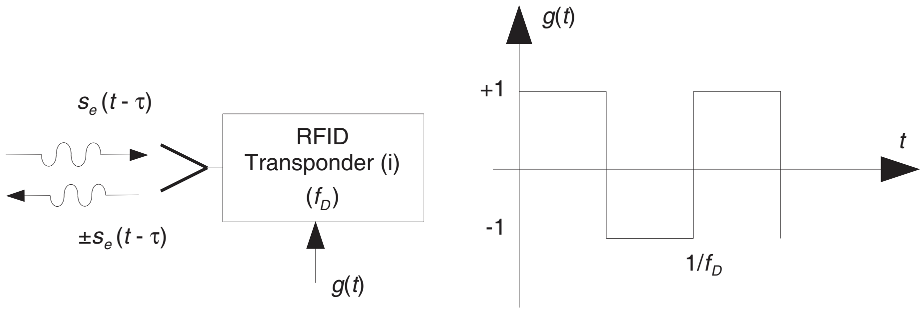

(a) (b)

Figure 15. Modeling the behavior of the nonlinear transponder.

where the complex coefficient C_n is given by

$$C_n = f_D \int_0^{1/f_D} g(t)\exp(-j2\pi n f_D t)dt = \frac{2}{j\pi n}, \quad (n \text{ odd}) \tag{20}$$

For $\tau_{\max} < t = t_c < T$ where t_c designates the short time variable (see Fig. 8), the signal received by the reader (primary radar) is given by

$$s_r(t) = g(t) \cdot s_e(t-\tau). \tag{21}$$

Finally, for $t = t_c + t_l$ where $t_l = mT$ (see Fig. 8), the expression of the beat signal becomes

$$s_b(t_c, t_l) = g(t_c + t_l) \cdot \exp\left(j2\pi(f_b t_c + \phi_0)\right). \tag{22}$$

Details of calculation are given in Appendix C.

As mentioned in Section 2.1 (Equation (9)), the Poisson formula is used to connect the two-dimensional Fourier transform $S_b(f, f')$ of the sampled beat signal (according to F_e and F_s) and that of the two-dimensional Fourier $S_b^c(f, f')$. Using the expression (19), $S_b(f, f')$ can be written as follows

$$S_b(f, f') = F_e F_s \sum_{n=-\infty}^{\infty} \sum_{k=-\infty}^{\infty} S_b^c(f - nF_e,\, f' - kF_s) \tag{23}$$

Since an anti-aliasing filter is applied in range frequency, the first term nF_e is omitted, and the expression can be reduced as follows:

$$\begin{aligned} S_b(f, f') &= F_e F_s \sum_{k=-\infty}^{\infty} S_b^c(f, f' - kF_s) \\ &= F_e F_s e^{j2\pi\phi'_0}(M-1)T(T-\tau_{\max}) \sum_{k=-\infty}^{\infty} \sum_{n=-\infty}^{\infty} C_n \\ &\quad \times e^{-j\pi(f'-kF_s-nf_D)(M-1)T} \operatorname{sinc}\left(\pi(f'-kF_s-nf_D)(M-1)T\right) \\ &\quad \times e^{-j\pi(f-f_b-nf_D)(T+\tau_{\max})} \operatorname{sinc}\left(\pi(f-f_b-nf_D)(T-\tau_{max})\right). \end{aligned} \tag{24}$$

Details of calculation are given in Appendix D.

Figure 16 shows the range-shift frequency cartography as the spectrum magnitude of the function (24) where the variable f represents the beat frequency, i.e., the target position, and f' the shift frequency. The spectrum magnitude corresponds to the configuration where the transponder is located

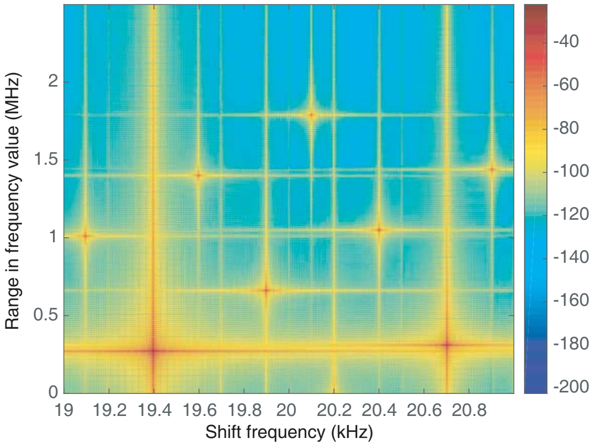

Figure 16. Two-dimensional discrete-time Fourier where sampling frequencies are $F_e = 20\,\text{MHz}$ and $F_s = 12.5\,\text{kHz}$. The shift frequency of the nonlinear transponder is $f_D = 19.4\,\text{kHz}$. The intervals are [0, 2.5 MHz] for the distance and [19 kHz, 21 kHz] for the shift frequency.

at the distance 50 m meaning that $f_b = 250\,\text{kHz}$ according to Equation (5), and the shift frequency $f_D = 19.4\,\text{kHz}$. Moreover, the spectrum has several harmonics due to the aliasing effect according to shift frequencies since we use the interval between 12.5 kHz and 25 kHz. In our application, the cutoff frequency of 3 MHz is used for the anti-aliasing filter, that does not allow aliasing in the [0, 3 MHz] band and does not induce effect to the range response.

Nevertheless, considering Fig. 16, many harmonics are detected along the shift frequency that corresponds to the nonlinear transponder behavior. It is obvious that these harmonics are not connected to any transponder. These harmonics correspond to the maximums reached by the functions $\text{sinc}\{\pi(f - f_b - nf_D)(T - \tau_{\max})\}$ and $\text{sinc}\{\pi(f' - kF_s - nf_D)(M-1)T\}$ for frequencies $f = f_b + nf_D$ and $f' = kF_s + nf_D$. These harmonics increase the false alarm rate that is dramatically useless for a detection system as GESTAR.

Table 4 gives the position of these points as a function of (k, n). On the one hand, the real position of the transponder is that of the position of the fundamental characterized by $(k, n) = (0, 1)$ with range frequency $f = f_b + f_D = 269.4\,\text{kHz}$, meaning that the detected range is 54.01 m, and the shift frequency $f' = f_D = 19.4\,\text{kHz}$. The position along the shift frequency axis is correct, but the range value is biased by an additional frequency f_D. We recall that this bias frequency is compensated by removing 20 kHz from the total beat frequency. On the other hand, the harmonics visible in the magnitude of the spectrum and caused by the nonlinear transponder behavior strongly affect the detection and the location of the real targets because they are considered themselves as targets and then give erroneous interpretations. The solution to this problem is to suppress these harmonics by calculating their positions. In the following subsection, we present a solution to remove the harmonics.

Table 4. Coordinates of all points of the range-shift frequency cartography as a function of (k, n) values. The frequency $f_b = 250\,\text{kHz}$ corresponds to a target at a distance $R = 50\,\text{m}$.

(k, n)	(0, 1)	(−3, 3)	(−31, 21)	(−59, 39)	(−62, 41)	(−90, 59)	(−93, 61)	(−121, 79)
$kF_s + nf_D$ (kHz)	19.4	20.7	19.9	19.1	20.4	19.6	20.9	20.1
$f_b + nf_D$ (kHz)	269.4	308.2	657.4	1006.6	1045.4	1394.6	1433.4	1782.6

5.2. Simulation of Removing Undesirable Harmonics

To remove the aliasing effects that induce false alarms, we propose to modify the modulation time T. Indeed, from the expression of the bidimensional Fourier transform $S_b(f, f')$ of the beat signal given by Equation (24), the position of the harmonics depends on the modulation time $T = 1/F_s$. The idea is to use several values of modulation time T and then to multiply two or more range-shift frequency cartographies corresponding to these different values of T. The fundamental frequency corresponding to the true target is retained by the product, and the harmonic frequencies are attenuated. It should be noted that the range resolution remains unchanged since it is given by $\Delta R = \frac{c}{2B}$ where B is the transmitted signal bandwidth. However, the shift frequency resolution changes since it is inversely proportional to the observation time of the processed signal $\Delta f_D = \frac{1}{MT}$ where M is the repetition number of the modulation time. To avoid a big change in the shift frequency resolution, the used modulation times are very close to each other. In this way, one does not affect too much the shift frequency resolution.

The proposed method is applied to various conditions, and some simulations are presented here. Fig. 17 shows two configurations of transponder location where the first position of the transponder is at $R = 12.5\,\text{m}$ from the reader and the second one at $R = 85\,\text{m}$. The shift frequency is the same for both configurations $f_D = 19.4\,\text{kHz}$. For $R = 12.5\,\text{m}$, each simulation corresponds to a different time modulation $T = \{80\,\mu\text{s}, 80.1\,\mu\text{s}, 80.2\,\mu\text{s}\}$. As shown in Figs. 17(a), (b) and (c), the harmonics are present in all the examples and may be confused with targets. As noted before, the positions of these harmonics correspond to the maximums reached by $S_b(f, f')$ for $f = f_b + nf_D$ and $f' = kF_s + nf_D$. It is clear that the multiplication of two or three images strongly attenuates the harmonics and retains only the fundamental that corresponds to the real target as shown in Fig. 17(d). For $R = 85\,\text{m}$, Figs. 17(e),

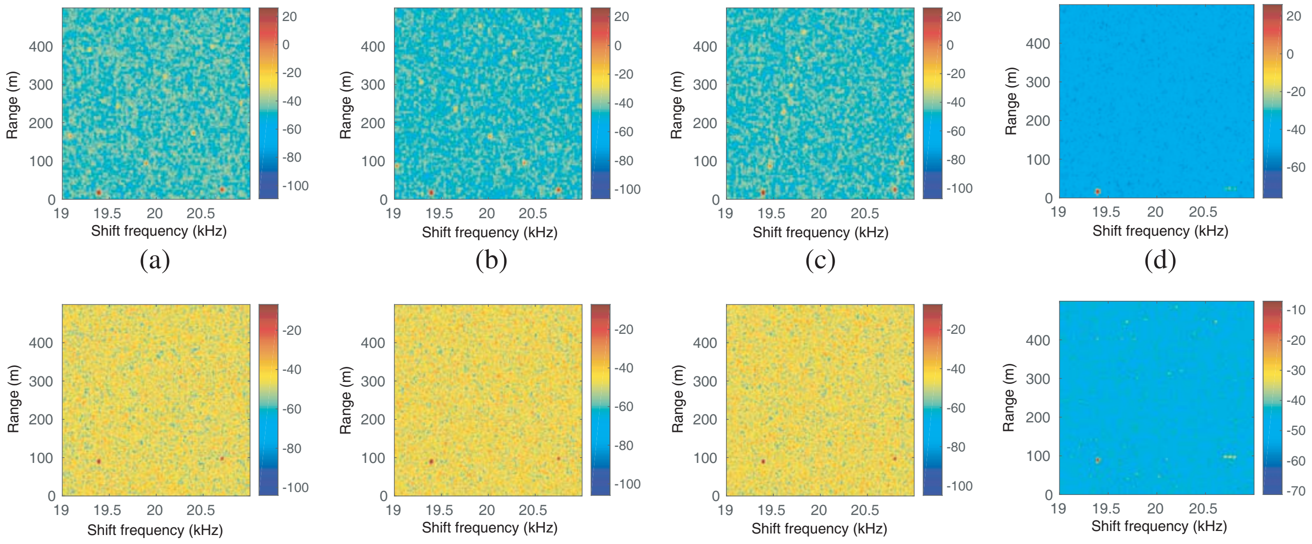

(a) (b) (c) (d)

(e) (f) (g) (h)

Figure 17. Simulations of range-shift frequency cartography with different modulation times $T = [80, 80.1, 80.2]$ µs given respectively in (a), (b) and (c). The first and second rows are defined for a distance $R = 12.5$ m and $R = 85$ m between transponder and reader, respectively. (a) $T = 80$ µs, (b) $T = 80.1$ µs, (c) $T = 80.2$ µs, (d) product

(f) and (g) show the same behavior but with less apparent harmonics due to more important magnitude of the noise power.

5.3. Indoor and Outdoor Measurements

Indoor measurement series are performed with the nonlinear transponder of the GESTAR project. We expose some curves describing range, shift frequency and orientation angle measurements. Fig. 18(a) shows the estimated range and the estimated shift frequency on indoor measurements that are performed 900 times. The estimated values of range and shift frequency which are respectively 30 m and 19.4 kHz correspond to the true values. Fig. 18(b) shows the estimated values of the orientation angle (blue color markers) with the real values of the angle (red color markers) with respect to the distance between the

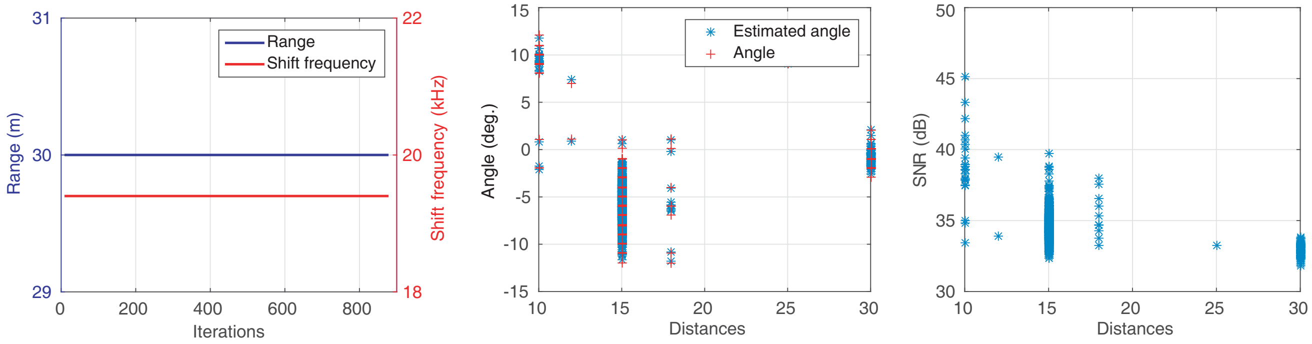

(a) (b) (c)

Figure 18. Range, shift frequency and orientation angle measurements. (a) Estimation of the distance separating the transponder from the radar and the shift frequency. (b) Angle of orientation of the transponder as a function of its position relative to the transponder. The red color corresponds to the true angle values and the blue color to the estimated values. (c) Evolution of the SNR (dB) as a function of the distance between the transponder and the reader.

reader and the transponder. We have to note that the angle assessments are close to the true value of the angle for distance values between 10 m and 30 m (indoor configuration). Fig. 18(c) shows the values of the SNR according to the number of measurements and with respect to the distance between the reader and the transponder. Also, the SNR decrease is seen as an expected phenomena.

Outdoor measurement series are carried out in an open place as shown in Fig. 19. The transponder is placed directly in front of the radar at different ranges and with different offset angles ranging from 0 radian to 0.3 radian. The shift frequency of the transponder is set at $f_D = 19.4\,\text{kHz}$. Table 5 describes different configurations for the transponder positions (range and angle) and gives the estimated distances, angles and shift frequency. We also measure the received signal power to evaluate the received power with respect to the range and offset angle which gives the location of the transponder with the relation to the reader one. According to the table, we can note that the estimated shift frequency is the same as the real shift frequency which characterizes the transponder. Moreover, the estimated ranges are close to the ground truth distances between the transponder and the reader. The error rate

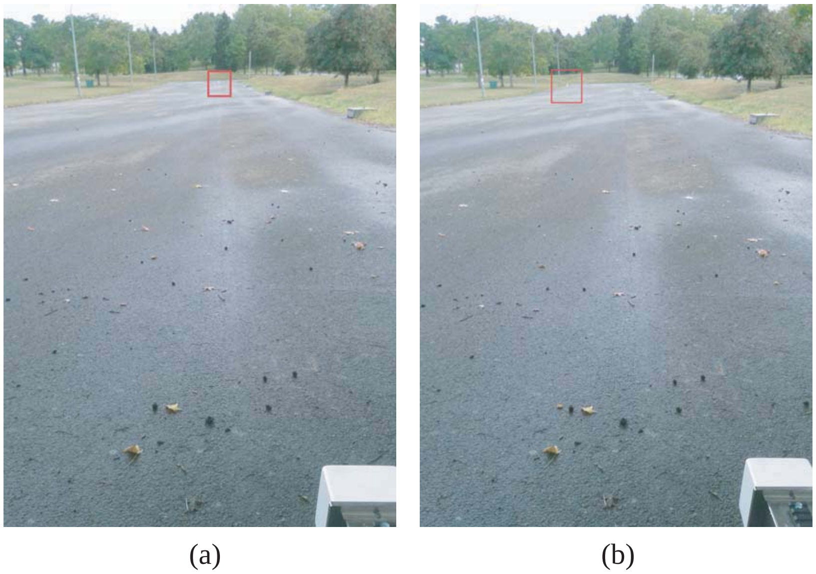
(a) (b)

Figure 19. Transponder position with respect to the reader. (a) The transponder is in front of the reader ($\theta = 0$ radian) and (b) slightly offset ($\theta = 0.1$ radian).

Table 5. Comparison between the ground truth values and the assessed parameters (angles and ranges). Measurements of shift frequencies and received signal power are added.

Ground thruth		Measurements			
Angle θ (rad)	Range R (m)	Angle estimation (rad)	Range estimation (m)	Shift frequency estimation (kHz)	Signal to noise ratio (dB)
0	139.6	0.0001	135	19.4	39.17
	115.1	−0.0002	117.5	19.4	37.48
	83.4	0.0001	85	19.4	42.23
	52.1	0.0000	52.5	19.4	48.53
0.1053	115.74	0.0958	117.5	19.4	35.95
	52.9	0.1564	52.5	19.4	46.42
0.1946	117.31	0.0075	120	19.4	28.81
0.3015	120.54	0.0024	125	19.4	16.74

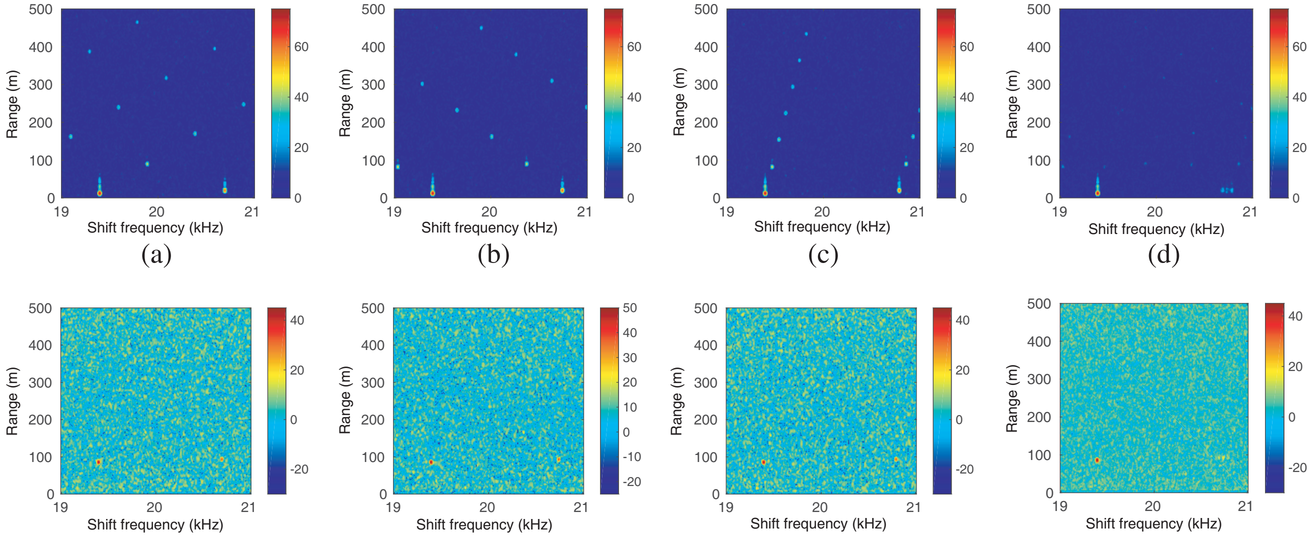

(a) (b) (c) (d)

(e) (f) (g) (h)

Figure 20. Range-shift frequency cartography provided from real measurements for two configurations of distance $R = 12.5\,\text{m}$ (first row) and $R = 85\,\text{m}$ (second row) and with different modulation times $T = \{80, 80.1, 80.2\}\,\mu\text{s}$. The figure (d) is the product of range-shift frequency cartographies given by (a), (b) and (c). The figure (h) is the product of range-shift frequency cartographies given by (e), (f) and (g). (a) $T = 80\,\mu\text{s}$, (b) $T = 80.1\,\mu\text{s}$,(c) $T = 80.2\,\mu\text{s}$, (d) product, (e) $T = 80\,\mu\text{s}$, (f) $T = 80.1\,\mu\text{s}$, (g) $T = 80.2\,\mu\text{s}$, (h) product.

is low for short distances and increases as distance increases. The angle assess remains reliable both for near-zero orientation angles and for small distances up to 52.5 m. In Fig. 20, we show range-shift frequency cartographies provided by the radar system for three modulation times for two transponder positions: $R = 12.5\,\text{m}$ and $R = 85\,\text{m}$.

It is clear that we have the same behavior with the simulations exhibited in Fig. 17, i.e., the same location of the harmonics. The product of these cartographies realized for different modulation times makes possible to attenuate the harmonics and to keep the fundamental that corresponds to the real target to be detected. Fig. 20(d) corresponds to the product of the range-shift frequency cartography of Figs. 20(a), (b) and (c). The same process is performed for Fig. 20(h).

6. CONCLUSION

In this paper, an FMCW radar system for RFID identification is presented. The range-shift frequency cartography and range-angular cartography are carried out from the spectral analysis of the beat signal. We define two kinds of transponder operations. We define a linear transponder when the shift frequency is linearly induced by the transmitted signal to the reader system. On the contrary, the shift frequency of a nonlinear transponder is nonlinearly added to the transmitted frequency. Also, the assessment of the performance of the systems are presented. A particular attention is given to the nonlinear transponder. The effects from the nonlinear behavior of the transponder on the beat frequency spectrum are studied. Furthermore, a signal processing procedure is proposed to mitigate and remove false alarms. The validation of the solutions is presented and validated based on simulated and real FMCW radar data. In perspective, we project the use of other transmitted waveforms as step frequency continuous wave (SFCW) in order to enhance the signal-to-noise ratio.

ACKNOWLEDGMENT

The authors would like to thank the DGA (Direction Générale de l'Armement) for funding this study.

APPENDIX A. BEAT SIGNAL DESCRIPTION

In the case of radar transponder configuration, we consider the transmitted signal which is described with

$$s_e(t) = \exp \jmath 2\pi \left(f_0 t + \frac{B}{2T} t^2 \right), \tag{A1}$$

and the received signal, which has been modified by a shift frequency modulation by the transponder device, is

$$s_r(t) = \exp \jmath 2\pi \left(f_0(t-\tau) + \frac{B}{2T}(t-\tau)^2 - f_D(t-\tau/2) \right) \tag{A2}$$

We have to note that the signal magnitude does not take into account the parameters included in the radar equation. After the homodyne demodulation, the beat signal $s_b(t) = s_e(t)s_r^*(t)$ is given as follows

$$\begin{aligned} s_b(t) &= \exp \jmath 2\pi \left(f_0 t + \frac{B}{2T} t^2 - f_0(t-\tau) - \frac{B}{2T}(t-\tau)^2 + f_D \left(t - \frac{\tau}{2} \right) \right) \\ &= \exp \jmath 2\pi \left(f_0 \tau - \frac{B}{2T}\tau^2 - f_D \frac{\tau}{2} + \frac{B}{T}\tau t + f_D t \right) \end{aligned} \tag{A3}$$

Let $\phi_0 = f_0\tau - (B\tau^2)/2T - f_D\tau/2$. Substituting ϕ_0 in the beat signal expression gives

$$s_b(t) = \exp \jmath 2\pi \left(\phi_0 + \frac{B}{T}\tau t + f_D t \right) \tag{A4}$$

Letting $t = t_c + mT$ with $m = 0, 1, \ldots, M-1$, the beat signal $s_b(t)$ over several cycles of wave replication is given with respect to the time axis t_c and mT

$$s_b(t) = \exp \jmath 2\pi \left(f_0\tau - \frac{B}{2T}\tau^2 - f_D\frac{\tau}{2} + B\tau m + \left(\frac{B}{T}\tau + f_D \right) t_c + f_D mT \right) \tag{A5}$$

Finally, we obtain

$$s_b(t) = e^{\jmath 2\pi(\phi_0 + B\tau m)} e^{\jmath 2\pi\left(\frac{B}{T}\tau + f_D\right)t_c} e^{\jmath 2\pi f_D mT} \tag{A6}$$

which is the beat signal expressed with Equation (6).

APPENDIX B. 2D FOURIER TRANSFORM OF THE BEAT SIGNAL

The bi-dimensional Fourier transform of the continuous beat signal $s_b^c(t_c, t_l)$ is given by

$$\begin{aligned} S_b^c(f, f') &= \int\limits_{\tau_{\max}}^{T} \int\limits_{0}^{(M-1)T} s_b^c(t_c, t_l) e^{-j2\pi f t_c} e^{-j2\pi f' t_l} dt_c dt_l \\ &= \int_0^{(M-1)T} \left(\int_{\tau_{\max}}^{T} s_b^c(t_c, t_l) e^{-j2\pi f t_c} dt_c \right) e^{-j2\pi f' t_l} dt_l \\ &= e^{j2\pi\phi_0} \left(\int_{\tau_{\max}}^{T} e^{-j2\pi(f-f_b)t_c} dt_c \right) \left(\int\limits_{0}^{(M-1)T} e^{-j2\pi(f'-f_D)t_l} dt_l \right) \end{aligned} \tag{B1}$$

The first integral is given as follows

$$\int_{\tau_{\max}}^{T} e^{-j2\pi(f-f_b)t_c} dt_c = (T - \tau_{\max}) e^{-j\pi(f-f_b)(T+\tau_{\max})} \times \operatorname{sinc}\left(\pi(f-f_b)(T-\tau_{\max})\right) \tag{B2}$$

In the same way

$$\int_0^{(M-1)T} e^{-j2\pi(f'-f_D)t_l} dt_l = (M-1)T e^{-j\pi(f'-f_D)(M-1)T} \times \operatorname{sinc}(\pi(f'-f_D)(M-1)T) \tag{B3}$$

So the expression of $S_b^c(f,f')$ is given by

$$\begin{aligned} S_b^c(f,f') &= e^{j2\pi\phi_0}(T-\tau_{\max})e^{-j\pi(f-f_b)(T+\tau_{\max})}\text{sinc}(\pi(f-f_b)(T-\tau_{\max})) \\ &\quad \times(M-1)Te^{-j\pi(f'-f_D)(M-1)T}\text{sinc}(\pi(f'-f_D)(M-1)T) \end{aligned} \tag{B4}$$

By using Poisson formula, we get (8).

APPENDIX C. BEAT SIGNAL TAKING INTO ACCOUNT NONLINEAR PONDERATION FUNCTION

$\forall t \in [0,(M-1)T[$, the transmitted signal is defined as follows

$$s_e(t) = \sum_{k=0}^{M-1} \exp j2\pi\left(f_0(t-kT)+\frac{B}{2T}(t-kT)^2\right)g'(t-kT) \tag{C1}$$

where $g'(t)=1$ for $t\in[0,T[$ and 0 otherwise. The received signal $s_r(t)$ is given $\forall t\in[0,(M-1)T[$ by

$$\begin{aligned} s_r(t) &= g(t)s_e(t-\tau) \\ &= g(t)\sum_{k=0}^{M-1}\exp j2\pi\left(f_0(t-\tau-kT)+\frac{B}{2T}(t-\tau-kT)^2\right)g'(t-\tau-kT) \end{aligned} \tag{C2}$$

The corresponding beat signal is given as follows

$$\begin{aligned} s_b(t) &= s_e(t).s_r^*(t) \\ &= \left(\sum_{k=0}^{M-1}\exp j2\pi\left(f_0(t-kT)+\frac{B}{2T}(t-kT)^2\right)g'(t-kT)\right) \\ &\quad \times g(t)\sum_{l=0}^{M-1}\exp -j2\pi\left(f_0(t-\tau-lT)+\frac{B}{2T}(t-\tau-lT)^2\right)g'(t-\tau-lT) \\ &= g(t)\sum_{k=0}^{M-1}\exp j2\pi\left(f_0(t-kT)-f_0(t-\tau-kT)+\frac{B}{2T}(t-kT)^2-\frac{B}{2T}(t-\tau-kT)^2\right) \\ &\quad \times g'(t-kT)g'(t-\tau-kT) \\ &= g(t)\sum_{k=0}^{M-1}\exp j2\pi\left(f_0\tau-\frac{B}{2T}\tau^2+\frac{B}{T}\tau t-\frac{B}{T}\tau kT\right)g'(t-kT)g'(t-\tau-kT) \\ &= g(t)\sum_{k=0}^{M-1}\exp j2\pi\left(\phi_0+f_b(t-kT)\right)g'(t-kT)g'(t-\tau-kT) \end{aligned} \tag{C3}$$

with $f_b = B\tau/T$ and $\phi_0 = f_0\tau - B\tau^2/(2T)$. For $t = t_c + mT \in [mT,(m+1)T[$, the expression of beat signal is then given

$$s_b(t_c+mT) = g(t_c+mT)e^{j2\pi(\phi_0+f_bt_c)}g'(t_c)g'(t_c-\tau) \tag{C4}$$

We prefer to use a bi-dimensional signal of the beat signal given by the following expression

$$s_b(t_c,mT) = g(t_c+mT)e^{j2\pi(\phi_0+f_bt_c)}. \tag{C5}$$

APPENDIX D. FOURIER TRANSFORM OF THE NONLINEAR BEAT SIGNAL

The first Fourier transform of the beat signal $s_b^c(t_c,t_l)$ over $t_c\in[\tau_{\max},T]$ is given by

$$S_b^c(f,t_l) = e^{j2\pi\phi_0'}\int_{\tau_{\max}}^{T} g(t_c+t_l)e^{-j2\pi(f-f_b)t_c}dt_c \tag{D1}$$

where $g(\cdot)$ is defined according (19). The last integral is evaluated as follows

$$\begin{aligned}\int_{\tau_{\max}}^{T} g(t_c+t_l)e^{-j2\pi(f-f_b)t_c}dt_c &= \sum_{n=-\infty}^{+\infty} C_n e^{j2\pi n f_D t_l}\int_{\tau_{\max}}^{T} e^{-j2\pi(f-f_b-nf_D)t_c}dt_c \\ &= (T-\tau_{\max})\sum_{n=-\infty}^{+\infty} C_n e^{j2\pi n f_D t_l} e^{-j\pi(f-f_b-nf_D)(T+\tau_{\max})} \\ &\quad \times \mathrm{sinc}\left(\pi(f-f_b-nf_D)(T-\tau_{\max})\right) \qquad \text{(D2)}\end{aligned}$$

Then, $S_b^c(f,t_l)$ can be written according to the above

$$\begin{aligned}S_b^c(f,t_l) &= e^{j2\pi\phi'_0}(T-\tau_{\max})\sum_{n=-\infty}^{+\infty} C_n e^{j2\pi n f_D t_l} \\ &\quad \times e^{-j\pi(f-f_b-nf_D)(T+\tau_{\max})}\mathrm{sinc}\left(\pi(f-f_b-nf_D)(T-\tau_{\max})\right) \qquad \text{(D3)}\end{aligned}$$

The second Fourier Transform of $S_b^c(f,t_l)$, this time, over t_l is given by

$$\begin{aligned}S_b^c(f,f') &= \int_0^{(M-1)T} S_b(f,t_l)e^{-j2\pi f' t_l}dt_l \\ &= e^{j2\pi\phi'_0}(T-\tau_{\max})\sum_{n=-\infty}^{+\infty} C_n e^{-j\pi(f-f_b-nf_D)(T+\tau_{\max})} \\ &\quad \times \mathrm{sinc}\left(\pi(f-f_b-nf_D)(T-\tau_{\max})\right)\int_0^{(M-1)T} e^{-j2\pi(f'-nf_D)t_l}dt_l \\ &= e^{j2\pi\phi'_0}(T-\tau_{\max})\sum_{n=-\infty}^{+\infty} C_n e^{-j\pi(f-f_b-nf_D)(T+\tau_{\max})} \\ &\quad \times \mathrm{sinc}\left(\pi(f-f_b-nf_D)(T-\tau_{\max})\right)(M-1)T \\ &\quad \times e^{-j\pi(f'-nf_D)(M-1)T}\mathrm{sinc}\left(\pi(f'-nf_D)(M-1)T\right) \qquad \text{(D4)}\end{aligned}$$

Finally, we can deduce Equation (24).

REFERENCES

1. Stove, A. G., "Linear FMCW radar techniques," *IEE Proceedings F (Radar and Signal Processing)*, Vol. 139, No. 5, 343–350, 1992.
2. Ting, J. W., D. Oloumi, and K. Rambabu, "FMCW SAR system for near-distance imaging applications-practical considerations and calibrations," *IEEE Transactions on Microwave Theory and Techniques*, Vol. 66, No. 1, 450–461, 2018.
3. McGregor, J. A., E. M. Poulter, and M. J. Smith, "Switching system for single antenna operation of an S-band FMCW radar," *Proceedings — Radar, Sonar and Navigation*, Vol. 141, No. 4, 241–248, 1994.
4. Butler, W., P. Poitevin, and J. Bjomholt, "Benefits of wide area intrusion detection systems using FMCW radar," *41st Annual IEEE International Carnahan Conference on Security Technology*, 176–182, 2007.
5. Galin, N., A. Worby, T. Markus, C. Leuschen, and P. Gogineni, "Validation of airborne FMCW radar measurements of snow thickness over sea ice in antarctica," *IEEE Transactions on Geoscience and Remote Sensing*, Vol. 50, No. 1, 3–12, 2012.
6. Iglesias, R., A. Aguasca, X. Fabregas, J. J. Mallorqui, D. Monells, C. Lopez-Martinez, and L. Pipia Galin, "Ground-based polarimetric SAR interferometry for the monitoring of terrain displacement phenomena," *IEEE Journal of Selected Topics in Applied Earth Observations and Remote Sensing*, Vol. 8, No. 3, 994–1007, 2015.

7. Boukari, B., E. Moldovan, S. Affes, K. Wu, R. G. Bosisio, and S. O. Tatu, "Six-port FMCW collision avoidance radar sensor configurations," *Canadian Conference on Electrical and Computer Engineering*, 305–308, 2008.
8. Al-Alem, Y., L. Albasha, and H. Mir, "High-resolution on-chip S-band radar system using stretch processing," *IEEE Sensors Journal*, Vol. 16, No. 12, 4749–4759, 2016.
9. Wang, Y. and Y. Zheng, "An FMCW radar transceiver chip for object positioning and human limb motion detection," *IEEE Sensors Journal*, Vol. 17, No. 2, 236–237, 2017.
10. Ghattas, L., S. Méric, and C. Brousseau, "Performance assessment of FMCW radar processing for transponder identification," *European Radar Conference (EuRAD)*, 258–261, 2016.
11. Hazry, D., M. R. Sofian Muhammad, and S. Zairi, "Study of integration 2.4 GHz and 5.8 GHz in RFID tag," *International Conference on Man-Machine Systems (ICoMMS)*, 2009.
12. Omar, H. G., A. Khoshnaw, and W. Monnet, "Smart patient management, monitoring and tracking system using radio-frequency identification (RFID) technology," *IEEE EMBS Conference on Biomedical Engineering and Sciences (IECBES)*, 40–45, 2016.
13. Ulku, A., "The next generation in personnel/people tracking: Active RFID technology has allowed for enhanced security and safety," *IEEE Consumer Electronics Magazine*, Vol. 6, No. 4, 122–124, 2017.
14. Namjun, C., S. Seong-Jun, K. Sunyoung, K. Shiho, and Y. Hoi-Jun, "A 5.1-μW UHF RFID tag chip integrated with sensors for wireless environmental monitoring," *31st European Solid-State Circuits Conference (ESSCIRC)*, 279–282, 2005.
15. Heidrich, J., D. Brenk, J. Essel, G. Fischer, G. Weigel, and S. Schwarzer, "Local positioning with passive UHF RFID transponders," *IEEE MTT-S International Microwave Workshop on Wireless Sensing, Local Positioning, and RFID*, 2009.
16. Skolnik, M., *Radar Handbook*, McGraw-Hill, New-York, 2008.
17. Skolnik, M., *Introduction to Radar Systems*, McGraw-Hill, New-York, 1980.
18. Le Chevalier, F., *Principles of Radar and Sonar Signal Processing*, Artech House, Norwood (MA), 2002.
19. Piper, S. O., "Receiver frequency resolution for range resolution in homodyne FMCW radar," *Conference on National Telesystems Conference*, 169–173, 1993.
20. Harris, F. J., "On the use of windows for harmonic analysis with the discrete Fourier transform," *Proceedings of the IEEE*, Vol. 66, No. 1, 51–83, 1978.
21. Rabiner, L., "The chirp Z-transform algorithm — A lesson in serendipity," *IEEE Signal Processing Magazine*, Vol. 21, No. 2, 118–119, 2004.
22. Rabiner, L., R. Schafer, and C. Rader, "The chirp Z-transform algorithm," *IEEE Transactions on Audio and Electroacoustics*, Vol. 17, No. 2, 86–92, 1969.